

A Neural-Network Extraction of Unpolarised Transverse-Momentum-Dependent Distributions

The MAP (Multi-dimensional Analyses of Partonic distributions) Collaboration

Alessandro Bacchetta,^{1,2,*} Valerio Bertone,^{3,†} Chiara Biscolotti,^{4,‡} Matteo Cerutti,^{5,6,§} Marco Radici,^{2,¶} Simone Rodini,^{7,**} and Lorenzo Rossi^{8,9,††}

¹*Dipartimento di Fisica, Università di Pavia, via Bassi 6, I-27100 Pavia, Italy*

²*INFN - Sezione di Pavia, via Bassi 6, I-27100 Pavia, Italy*

³*IRFU, CEA, Université Paris-Saclay, F-91191 Gif-sur-Yvette, France*

⁴*Argonne National Laboratory, PHY Division, Lemont, IL, USA*

⁵*Hampton University, Hampton, Virginia 23668, USA*

⁶*Jefferson Lab, Newport News, Virginia 23606, USA*

⁷*Deutsches Elektronen-Synchrotron DESY, Notkestr. 85, 22607 Hamburg, Germany*

⁸*Dipartimento di Fisica, Università di Milano, Via Celoria 16, 20133 Milan, Italy*

⁹*INFN, Sezione di Milano, Via Celoria 16, 20133 Milan, Italy*

We present the first extraction of transverse-momentum-dependent distributions of unpolarised quarks from experimental Drell-Yan data using neural networks to parametrise their nonperturbative part. We show that neural networks outperform traditional parametrisations providing a more accurate description of data. This work establishes the feasibility of using neural networks to explore the multi-dimensional partonic structure of hadrons and paves the way for more accurate determinations based on machine-learning techniques.

Introduction

Transverse-momentum-dependent (TMD) distributions provide an important window to investigate the partonic structure of hadrons, enabling a deeper understanding of the three-dimensional dynamics of quarks and gluons within them. TMDs consist of both perturbative and nonperturbative components. While the perturbative part can be calculated from first principles using Quantum Chromodynamics (QCD), the nonperturbative part, which encapsulates long-distance physics, by definition cannot be evaluated using perturbative methods and must be extracted from experimental data. An accurate parametrisation of the nonperturbative contribution to TMDs is therefore essential for reliable extractions. The abundance of experimental measurements and the development of a robust theoretical framework have favoured a remarkable progress of TMD studies in recent years. Indeed, accurate phenomenological extractions for unpolarised quark TMDs in the proton are now available [1–9].

Despite this active research landscape, explorations of different parametrisations of the TMD nonperturbative part were limited to models based on a small set of functions, such as exponentials and (weighted) Gaussians. While these parametrisations are effective, they carry a significant bias that may limit the accuracy of the models. This rigidity can hinder the ability to fully capture the underlying physics and extract information from experimental data. To overcome these limitations, a promising alternative is given by neural networks (NNs).

In this work, we present the first extraction of the unpolarised quark TMD parton distribution functions (PDFs) in the proton using NNs to parametrise their

nonperturbative component, achieving next-to-next-to-next-to-leading logarithmic (N³LL) accuracy. This constitutes a proof-of-concept extraction, as it is based on Drell-Yan (DY) production data only and neglects flavour dependence of the intrinsic transverse momentum of quarks. Nevertheless, it demonstrates that NN-based TMD extractions outperform traditional nonperturbative parametrisations. Indeed, we provide evidence that current experimental data encode complexities beyond the reach of traditional parametrisations. We remark that NNs have been used in the past to study other partonic distributions (see, *e.g.*, Refs. [10–14]), but never unpolarised TMDs. Our work paves the way for improved TMD extractions, leveraging the flexibility of NNs to extract information on the multidimensional structure of hadrons using data from current and future experiments.

Formalism and parametrisation

We consider the DY process $h_A + h_B \rightarrow \ell^+ + \ell^- + X$ where two hadrons with mass M and four-momenta P_A and P_B collide with center-of-mass energy squared $s = (P_A + P_B)^2$, and inclusively produce a lepton pair with total four-momentum q and invariant mass $Q \gg M$. If the transverse momentum component \mathbf{q}_T with respect to the collision axis satisfies the condition $|\mathbf{q}_T| \equiv q_T \ll Q$,

the differential cross section can be written as

$$\begin{aligned} \frac{d\sigma^{\text{DY}}}{dq_T dy dQ} &= \frac{8\pi\alpha^2 q_T}{9Q^3} \mathcal{P} x_A x_B \mathcal{H}^{\text{DY}}(Q, \mu) \sum_a c_a(Q^2) \\ &\times \int_0^\infty db_T b_T J_0(b_T q_T) \hat{f}_1^a(x_A, b_T^2; \mu, \zeta_A) \hat{f}_1^{\bar{a}}(x_B, b_T^2; \mu, \zeta_B), \end{aligned} \quad (1)$$

where $y = \ln \sqrt{(q_0 + q_z)/(q_0 - q_z)}$ is the lepton-pair rapidity, α is the electromagnetic coupling, \mathcal{P} is a phase-space-reduction factor accounting for possible lepton cuts,¹ $x_{A,B} = Qe^{\pm y}/\sqrt{s}$ are the longitudinal momentum fractions carried by the incoming quarks, \mathcal{H}^{DY} is a perturbative hard factor encoding the virtual part of the scattering, and the sum runs over all active quark flavours a with c_a the quark electroweak charges.

In Eq. (1), \hat{f}_1^a is the Fourier transform of the unpolarised TMD PDF of quark flavour a . It depends on the quark longitudinal momentum fraction x and on the variable $b_T = |\mathbf{b}_T|$, where \mathbf{b}_T is Fourier-conjugated to the quark intrinsic transverse momentum \mathbf{k}_\perp . It also depends on the renormalisation scale μ and on the rapidity scale ζ (with the constraint $\zeta_A \zeta_B = Q^4$). Such dependence arises from the removal of ultraviolet and rapidity divergences [15] and is controlled by corresponding evolution equations. The complete set of equations (omitting unessential variables and indices) is given by

$$\begin{aligned} \frac{\partial \hat{f}_1}{\partial \ln \mu} &= \gamma(\mu, \zeta), & \frac{\partial \hat{f}_1}{\partial \ln \sqrt{\zeta}} &= K(\mu), \\ \frac{\partial K}{\partial \ln \mu} &= \frac{\partial \gamma}{\partial \ln \sqrt{\zeta}} = -\gamma_K(\alpha_s(\mu)), \end{aligned} \quad (2)$$

where γ and K are the anomalous dimensions of renormalisation group and of Collins-Soper equations, respectively, and γ_K is the so-called cusp anomalous dimension which relates the cross derivatives of \hat{f}_1 .

Given a set of initial scales (μ_i, ζ_i) , the solution to these differential equations allows us to determine the \hat{f}_1 at any final scales (μ_f, ζ_f) . In addition, in the region of small transverse separations b_T , the TMD PDF \hat{f}_1 can be matched onto unpolarised *collinear* PDFs f_1 through a convolution with perturbatively calculable matching coefficients C .

The resulting expression for the TMD PDF at the final scales (μ_f, ζ_f) is

$$\begin{aligned} \hat{f}_1(x, b_T; \mu_f, \zeta_f) &= [C \otimes f_1](x, b_T; \mu_i, \zeta_i) \\ &\times \exp \left\{ K(\mu_i) \ln \frac{\sqrt{\zeta_f}}{\sqrt{\zeta_i}} \right. \\ &\left. + \int_{\mu_i}^{\mu_f} \frac{d\mu}{\mu} \left[\gamma_F(\alpha_s(\mu)) - \gamma_K(\alpha_s(\mu)) \ln \frac{\sqrt{\zeta_f}}{\mu} \right] \right\}, \end{aligned} \quad (3)$$

where $\gamma_F(\alpha_s(\mu)) = \gamma(\mu, \mu^2)$ and \otimes indicates the Mellin convolution over the longitudinal momentum fraction x . A convenient choice for the initial scales is $\mu_i = \sqrt{\zeta_i} \equiv \mu_b = 2e^{-\gamma_E}/b_T$, with γ_E the Euler constant, in that it avoids the resurgence of large logarithms in the anomalous dimension K and in the matching coefficients C .

The TMD PDF in Eq. (3) includes the resummation of large logarithms of b_T to all orders in perturbation theory. A given logarithmic accuracy implies that each ingredient in Eq. (3) must be computed to the appropriate perturbative accuracy. The present extraction incorporates all the necessary ingredients to reach N³LL accuracy [3].

The introduction of the scale $\mu_b \sim 1/b_T$ requires a prescription to avoid integrating in Eq. (1) over the QCD Landau pole (Λ_{QCD}) in the large- b_T region. To this purpose, we adopt the same choice of Refs. [1, 5, 7, 9, 16] and replace μ_b with $\mu_{b_*} = 2e^{-\gamma_E}/b_*$, where

$$b_*(b_T, b_{\min}, b_{\max}) = b_{\max} \left(\frac{1 - e^{-b_T^4/b_{\max}^4}}{1 - e^{-b_T^4/b_{\min}^4}} \right)^{1/4}, \quad (4)$$

with

$$b_{\max} = 2e^{-\gamma_E} \text{ GeV}^{-1} \quad b_{\min} = 2e^{-\gamma_E}/\mu_f. \quad (5)$$

This choice guarantees that the variable b_* rapidly saturates to b_{\max} at large values of b_T , preventing μ_{b_*} from reaching Λ_{QCD} . However, b_* also introduces spurious power corrections that scale like $(\Lambda_{\text{QCD}}/q_T)^k$ [17–20], with $k > 0$. In the region $q_T \simeq \Lambda_{\text{QCD}}$, these power corrections become sizeable and can be modelled by including in Eq. (3) the nonperturbative function f_{NP} as follows:

$$\begin{aligned} \hat{f}_1(x, b_T; \mu_f, \zeta_f) &= [C \otimes f_1](x, b_T; \mu_{b_*}, \mu_{b_*}^2) \\ &\times \exp \left\{ K(b_*, \mu_{b_*}) \ln \frac{\sqrt{\zeta_f}}{\mu_{b_*}} \right. \\ &\left. + \int_{\mu_{b_*}}^{\mu_f} \frac{d\mu}{\mu} \left[\gamma_F(\alpha_s(\mu)) - \gamma_K(\alpha_s(\mu)) \ln \frac{\sqrt{\zeta_f}}{\mu} \right] \right\} \\ &\times f_{\text{NP}}(x, b_T; \zeta_f). \end{aligned} \quad (6)$$

The nonperturbative function must satisfy the condition $f_{\text{NP}} \rightarrow 1$ for $b_T \rightarrow 0$ in order to recover the perturbative regime. It must also grant that the TMD PDF is suppressed for large values of b_T and ζ_f . We parametrise f_{NP} using a NN but enforcing these physically required constraints. We explored several different NN parametrisations and will report on them in a future work. As a proof of concept, in this work we focus on the following model:

$$f_{\text{NP}}(x, b_T; \zeta) = \frac{\text{NN}(x, b_T)}{\text{NN}(x, 0)} \exp \left[-g_2^2 b_T^2 \log \left(\frac{\zeta}{Q_0^2} \right) \right], \quad (7)$$

where, as customary, we split f_{NP} into an ‘‘intrinsic’’ nonperturbative part, entirely parametrised by the NN (denoted as NN), and the nonperturbative contribution to

¹ See Appendix C of Ref. [5] for details.

the rapidity evolution, encoded in the exponential function. The NN is taken with architecture [2, 10, 1], *i.e.* with two inputs corresponding to x and b_T , 10 hidden nodes, and one output node. The activation function associated to the nodes of the hidden layer is

$$\sigma(z) = \frac{1}{2} \left(1 + \frac{z}{1 + |z|} \right), \quad (8)$$

which resembles the more traditional sigmoid function but offers a significant reduction of computational burden while granting an excellent quality of the final result. The activation function for the outer layer is instead chosen to be quadratic. The reference scale for the rapidity evolution is set to $Q_0 = 1$ GeV. The parametrisation of the function f_{NP} in Eq. (7) is engineered to match the constraints mentioned above, namely $f_{\text{NP}} \rightarrow 1$ for $b_T \rightarrow 0$ and $f_{\text{NP}} \ll 1$ for large b_T and ζ_f . With this setup, we have a total of 42 free parameters, 41 associated to the NN and one (g_2) to the evolution.

The values of the best-fit parameters are obtained by minimising a χ^2 that accounts for all sources of experimental uncertainties. The minimisation is performed using the Levenberg–Marquardt algorithm as implemented in the `Ceres-Solver` package [21]. An important aspect of our analysis is that the gradient of the χ^2 with respect to the free parameters is evaluated *analytically* by exploiting the ability to compute the derivatives of the NN with respect to its parameters in a closed form [22]. This feature is crucial to ensure a fast and stable convergence of the minimisation procedure.

Finally, overfitting is a well known problem of phenomenological analyses based on NNs [23, 24]. We avoid it by using the cross-validation method [25]. Specifically, the data set is split into two subsets: one for training and one for validation. The training set is used to determine the best-fit parameters, while the validation set is used to monitor the quality of the fit. The best-fit set of parameters is determined by requiring the χ^2 of the validation set to be minimal. In our analysis, we divided the data set into validation and training sets of the same size.

Results

In this section, we discuss the results for the fit of f_{NP} in Eq. (7) to the DY experimental data included in the most recent analyses of the MAP Collaboration (see Refs. [7, 9] for more details). We consider fixed-target data from Fermilab (E605 [26], E288 [27], and E772 [28]) and collider data from Tevatron (CDF [29, 30], D0 [31–33]), RHIC (STAR [34]), and the LHC (LHCb [35–37], CMS [38–40], ATLAS [41–43]).

The collinear PDFs f_1 in Eq. (6) are taken from the MSHT2020 set [44] of the LHAPDF library [45] at next-to-next-to-leading-order, which is necessary to achieve

N³LL. The strong coupling α_s is obtained from the same PDF set. We propagate the uncertainties of collinear PDFs into TMD PDFs as in Refs. [7, 16]. In order to ensure applicability of TMD factorisation, we impose the kinematic cut $q_T/Q < 0.2$. We exclude all experimental data in the energy range of the Υ resonance (9 GeV $< Q < 11$ GeV). Moreover, we neglect the PHENIX data of Ref. [46], originally included in the analyses of Refs. [7, 9], because only two data points survive the q_T/Q cut and their description is typically poor for any parametrisation of f_{NP} .

The propagation of the experimental uncertainties into the TMD PDFs is achieved through Monte Carlo (MC) sampling: an ensemble of $N_{\text{rep}} = 250$ fluctuations (replicas) of the experimental data set is generated accounting for correlated uncertainties, and each replica is used to extract f_{NP} .

In order to estimate the performance of our NN-based fit, we performed an additional fit with the same settings (data set, perturbative order, etc.) but parametrising f_{NP} with the functional form used in Ref. [7], which features 12 free parameters. In Tab. I, we compare the quality of the NN-based fit with this latter fit referred to as MAP22 (see Ref. [47] for the full results). For each data subset (fixed-target, RHIC, Tevatron, ATLAS, CMS, and LHCb) we list the number of points included in the fit (N_{dat}) and the reduced $\bar{\chi}^2$ ($= \chi^2/N_{\text{dat}}$) of the central replica, *i.e.* the fit to the experimental central values without MC fluctuations. The total $\bar{\chi}^2$ is given in the bottom line. For each $\bar{\chi}^2$ value, we also provide separately uncorrelated ($\bar{\chi}_D^2$) and correlated ($\bar{\chi}_\lambda^2$) contributions (see Appendix B of Ref. [3] for more details).

Experiment	N_{dat}	$\bar{\chi}^2$ ($\bar{\chi}_D^2 + \bar{\chi}_\lambda^2$)	
		NN	MAP22
Fixed-target	233	1.08 (0.98 + 0.10)	0.91 (0.70 + 0.21)
RHIC	7	1.11 (1.03 + 0.07)	1.45 (1.37 + 0.08)
Tevatron	71	0.80 (0.73 + 0.06)	1.20 (1.17 + 0.04)
LHCb	21	0.98 (0.88 + 0.10)	1.25 (1.05 + 0.20)
CMS	78	0.40 (0.38 + 0.02)	0.41 (0.35 + 0.06)
ATLAS	72	1.38 (1.09 + 0.29)	3.51 (3.03 + 0.49)
Total	482	0.97 (0.86 + 0.11)	1.28 (1.09 + 0.20)

TABLE I: Breakdown of the reduced $\bar{\chi}^2 = \chi^2/N_{\text{dat}}$ for each subset included in the fit and for the total data set. Results obtained with the parametrisation in Eq. (7) (NN) and that of Ref. [7] (MAP22) are shown. $\bar{\chi}_D^2$ and $\bar{\chi}_\lambda^2$ correspond to uncorrelated and correlated contributions to $\bar{\chi}^2$, respectively [3].

It is evident that the NN fit achieves a better description of data than MAP22, not only at the level of the global $\bar{\chi}^2$ (0.97 for NN vs. 1.28 for MAP22), but also for almost all single subsets (with the only exception of

fixed-target). Particularly significant is the improvement for ATLAS, for which the $\bar{\chi}^2$ value drops from 3.51 for MAP22 to 1.38 for NN. As the ATLAS measurements are the most precise ones, this is a clear indication that the NN parametrisation can better capture the information encoded in the data. We also note that the correlated contributions $\bar{\chi}^2_\lambda$ for the NN fit are generally smaller than for MAP22, *i.e.* the NN fit is able to describe the data without relying on large correlated shifts.

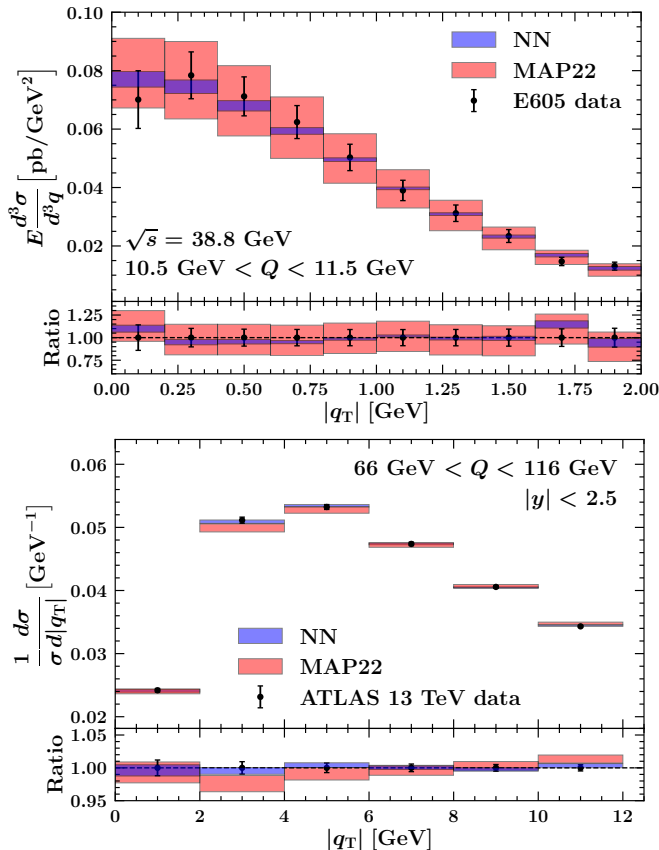


FIG. 1: Comparison between experimental data (black dots) and results obtained with NN (blue band) and MAP22 (red band) fits. The top plot displays the $10.5 \text{ GeV} < Q < 11.5 \text{ GeV}$ bin of the E605 data set, while the bottom plot displays the ATLAS measurements at 13 TeV. For each plot, upper and lower panels show the actual distributions and their ratios to the experimental central values, respectively. Theoretical uncertainty bands correspond to one- σ uncertainties, error bars on experimental data display uncorrelated uncertainties only.

A visual representation of this statement is given in Fig. 1, where we show a comparison between experimental data and results of the fit for a representative selection of data: a Q -bin from the fixed-target E605 experiment (top plot) and the ATLAS measurements at 13 TeV (bottom plot). Blue and red bands correspond to one- σ uncertainties of NN and MAP22 fits, respectively, while experimental data points are shown as black dots along

with their uncorrelated uncertainties. The upper panel of each plot displays the absolute distributions while the lower panel displays the distributions normalised to the experimental central values.

In Fig. 1, it is evident that uncertainty bands are significantly different between NN and MAP22 fits, with the former being generally smaller than the latter. This is a direct consequence of the larger systematic shifts that affect MAP22 (see Tab. I). This is especially evident for the E605 data where correlated uncertainties are particularly large. For the ATLAS data, the size of the bands is comparable because systematic shifts are bound to be small due to the small size of experimental uncertainties. We also observe that the NN fit tends to better reproduce the shape of the ATLAS data distribution.

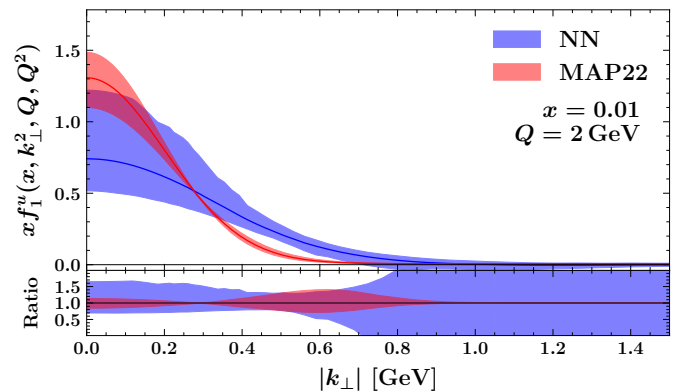


FIG. 2: The unpolarised TMD PDF of the u -quark in the proton extracted using the NN (blue) and the MAP22 (red) parametrizations at $\mu = \sqrt{\zeta} = 2 \text{ GeV}$ and $x = 0.01$ as functions of the quark transverse momentum $|k_\perp|$. The upper panel shows the actual distributions, while the bottom panel shows their ratios to the respective central values. Error bands represent one- σ uncertainties.

In Fig. 2, we show the unpolarised TMD PDF of the u -quark in the proton at $\mu = \sqrt{\zeta} = 2 \text{ GeV}$ and $x = 0.01$ as a function of the quark transverse momentum $|k_\perp|$. As before, blue and red bands correspond to NN and MAP22, respectively. The upper panel displays the actual TMD distributions, while in the lower panel they are normalised to the respective central values.

A generally good agreement between NN and MAP22 is observed, with the former featuring a larger relative uncertainty band. This is a direct consequence of the flexibility of the NN parametrisation. In this respect, it is interesting to observe that the relative size of the NN uncertainty band remains fairly stable up to $|k_\perp| \sim 0.6 \text{ GeV}$, while it tends to increase for larger values of $|k_\perp|$ because of the increasingly smaller central value. On the contrary, the MAP22 relative uncertainty band shrinks as $|k_\perp|$ increases. Moreover, it shows a node at intermediate values of $|k_\perp|$. This behaviour can be traced back to the rigidity of the parametrisation.

The fact that the NN TMD PDF has larger uncertainties than the MAP22 one may seem to contrast with the results shown in Fig. 1, where cross sections computed with the NN model display smaller uncertainties than MAP22. This can be understood by noting that during the minimisation process the greater flexibility of the NN model enables it to better adapt to the behaviour of data. Consequently, the minimiser does not need to resort to large correlated shifts to minimise the χ^2 , avoiding an inflation of the uncertainty in the final outcome.

Conclusions

In this work, we presented the first extraction of the unpolarised quark TMD PDFs in the proton from a comprehensive set of DY data using a parametrisation for the nonperturbative part based on a NN. Our results employ state-of-the-art perturbative inputs reaching N³LL accuracy, and leverage modern numerical techniques, such as MC sampling for uncertainty propagation, analytic computation of the gradient of the χ^2 for a more accurate exploration of the parameter space, cross-validation to avoid overfitting, and full treatment of correlated experimental uncertainties.

By directly comparing the results obtained with the NN parametrisation to those of the more traditional functional form of Ref. [7] (MAP22), we showed that the former is superior in terms of fit quality. This provides clear evidence that the NN-based parametrisation captures more effectively the information encoded in the data than traditional parametrisations. This is particularly evident for the ATLAS measurements, the most precise data sets included in the fit. We showed that the flexibility of the NN parametrisation allows us to better control the impact of correlated uncertainties. For data sets characterised by large correlated systematics, such as the fixed-target measurements, this typically leads to a significant reduction of uncertainties.

This work serves as a proof of concept, opening new and exciting possibilities for future high-precision and high-impact extractions. One of the main advantages of NNs is that they scale particularly well with the complexity of the task. More specifically, extending the data set to include semi-inclusive deep-inelastic scattering data (which in turn requires a simultaneous fit of TMD PDFs and TMD fragmentation functions) and introducing TMD flavour dependence is a relatively straightforward task when using NNs. We are currently working along these directions and plan to release a fully-fledged TMD extraction based on NNs in the near future.

Acknowledgments

The work of S.R. is supported by the German Science Foundation (DFG), grant number 409651613 (Research Unit FOR 2926), subproject 430915355. The work of L.R. is partially supported by the Italian Ministero dell'Università e Ricerca (MUR) through the research grant 20229KEFAM. This material is also based upon work supported by the U.S. Department of Energy, Office of Science, Office of Nuclear Physics under contract DE-AC05-06OR23177. The contribution of C.B. is based upon work supported by Laboratory Directed Research and Development (LDRD) funding from Argonne National Laboratory, provided by the Director, Office of Science, of the U.S. Department of Energy under Contract No. DE-AC02-06CH11357.

* E-mail: alessandro.bacchetta@unipv.it – ORCID: [0000-0002-8824-8355](https://orcid.org/0000-0002-8824-8355)

† E-mail: valerio.bertone@cea.fr – ORCID: [0000-0003-0148-0272](https://orcid.org/0000-0003-0148-0272)

‡ E-mail: cbissolotti@anl.gov – ORCID: [0000-0003-3061-0144](https://orcid.org/0000-0003-3061-0144)

§ E-mail: mcerutti@jlab.org – ORCID: [0000-0001-7238-5657](https://orcid.org/0000-0001-7238-5657)

¶ E-mail: marco.radici@pv.infn.it – ORCID: [0000-0002-4542-9797](https://orcid.org/0000-0002-4542-9797)

** E-mail: simone.rodini@desy.de – ORCID: [0000-0002-8057-5597](https://orcid.org/0000-0002-8057-5597)

†† E-mail: lorenzo.rossi3@unimi.it – ORCID: [0000-0002-8326-3118](https://orcid.org/0000-0002-8326-3118)

- [1] A. Bacchetta, F. Delcarro, C. Pisano, M. Radici, and A. Signori, *JHEP* **06**, 081 (2017), [Erratum: *JHEP* **06**, 051 (2019)].
- [2] I. Scimemi and A. Vladimirov, *Eur. Phys. J. C* **78**, 89 (2018).
- [3] V. Bertone, I. Scimemi, and A. Vladimirov, *JHEP* **06**, 028 (2019).
- [4] I. Scimemi and A. Vladimirov, *JHEP* **06**, 137 (2020).
- [5] A. Bacchetta, V. Bertone, C. Bissolotti, G. Bozzi, F. Delcarro, F. Piacenza, and M. Radici, *JHEP* **07**, 117 (2020).
- [6] M. Bury, F. Hautmann, S. Leal-Gomez, I. Scimemi, A. Vladimirov, and P. Zurita, *JHEP* **10**, 118 (2022).
- [7] A. Bacchetta, V. Bertone, C. Bissolotti, G. Bozzi, M. Cerutti, F. Piacenza, M. Radici, and A. Signori (MAP (Multi-dimensional Analyses of Partonic distributions)), *JHEP* **10**, 127 (2022).
- [8] V. Moos, I. Scimemi, A. Vladimirov, and P. Zurita, *JHEP* **05**, 036 (2024).
- [9] A. Bacchetta, V. Bertone, C. Bissolotti, G. Bozzi, M. Cerutti, F. Delcarro, M. Radici, L. Rossi, and A. Signori (MAP), *JHEP* **08**, 232 (2024).
- [10] M. Čuić, K. Kumerički, and A. Schäfer, *Phys. Rev. Lett.* **125**, 232005 (2020).
- [11] R. Abdul Khalek, V. Bertone, A. Khoudli, and E. R. Nocera (MAP (Multi-dimensional Analyses of Partonic distributions)), *Phys. Lett. B* **834**, 137456 (2022).
- [12] I. P. Fernando and D. Keller, *Phys. Rev. D* **108**, 054007

- (2023).
- [13] V. Bertone, A. Chiefa, and E. R. Nocera (MAP) (2024), arXiv:2404.04712 [hep-ph].
- [14] R. D. Ball et al. (NNPDF), *Eur. Phys. J. C* **84**, 659 (2024).
- [15] J. Collins, *Foundations of Perturbative QCD*, vol. 32 of *Cambridge Monographs on Particle Physics, Nuclear Physics and Cosmology* (Cambridge University Press, 2023), ISBN 978-1-009-40184-5, 978-1-009-40183-8, 978-1-009-40182-1.
- [16] M. Cerutti, L. Rossi, S. Venturini, A. Bacchetta, V. Bertone, C. Bissolotti, and M. Radici (MAP (Multi-dimensional Analyses of Partonic distributions)), *Phys. Rev. D* **107**, 014014 (2023).
- [17] S. Catani, M. L. Mangano, P. Nason, and L. Trentadue, *Nucl. Phys. B* **478**, 273 (1996).
- [18] A. Kulesza, G. F. Sterman, and W. Vogelsang, *Phys. Rev. D* **66**, 014011 (2002).
- [19] E. Laenen, G. F. Sterman, and W. Vogelsang, *Phys. Rev. Lett.* **84**, 4296 (2000).
- [20] A. Kulesza, G. F. Sterman, and W. Vogelsang, *Phys. Rev. D* **69**, 014012 (2004).
- [21] S. Agarwal, K. Mierle, and T. C. S. Team, *Ceres Solver* (2023), <https://github.com/ceres-solver/ceres-solver>.
- [22] R. Abdul Khalek and V. Bertone (2020), arXiv:2005.07039 [physics.comp-ph].
- [23] R. D. Ball et al. (NNPDF), *Eur. Phys. J. C* **77**, 663 (2017).
- [24] R. D. Ball et al. (NNPDF), *Eur. Phys. J. C* **82**, 428 (2022).
- [25] L. Del Debbio, S. Forte, J. I. Latorre, A. Piccione, and J. Rojo (NNPDF), *JHEP* **03**, 039 (2007).
- [26] G. Moreno et al., *Phys. Rev. D* **43**, 2815 (1991).
- [27] A. S. Ito et al., *Phys. Rev. D* **23**, 604 (1981).
- [28] P. L. McGaughey et al. (E772), *Phys. Rev. D* **50**, 3038 (1994), [Erratum: *Phys.Rev.D* 60, 119903 (1999)].
- [29] T. Affolder et al. (CDF), *Phys. Rev. Lett.* **84**, 845 (2000).
- [30] T. Aaltonen et al. (CDF), *Phys. Rev. D* **86**, 052010 (2012).
- [31] B. Abbott et al. (D0), *Phys. Rev. D* **61**, 032004 (2000).
- [32] V. M. Abazov et al. (D0), *Phys. Rev. Lett.* **100**, 102002 (2008).
- [33] V. M. Abazov et al. (D0), *Phys. Lett. B* **693**, 522 (2010).
- [34] S. Collaboration, *Phys. Lett. B* **854**, 138715 (2024).
- [35] R. Aaij et al. (LHCb), *JHEP* **08**, 039 (2015).
- [36] R. Aaij et al. (LHCb), *JHEP* **01**, 155 (2016).
- [37] R. Aaij et al. (LHCb), *JHEP* **09**, 136 (2016).
- [38] S. Chatrchyan et al. (CMS), *Phys. Rev. D* **85**, 032002 (2012).
- [39] V. Khachatryan et al. (CMS), *JHEP* **02**, 096 (2017).
- [40] A. M. Sirunyan et al. (CMS), *JHEP* **12**, 061 (2019).
- [41] G. Aad et al. (ATLAS), *JHEP* **09**, 145 (2014).
- [42] G. Aad et al. (ATLAS), *Eur. Phys. J. C* **76**, 291 (2016).
- [43] G. Aad et al. (ATLAS), *Eur. Phys. J. C* **80**, 616 (2020).
- [44] S. Bailey, T. Cridge, L. A. Harland-Lang, A. D. Martin, and R. S. Thorne, *Eur. Phys. J. C* **81**, 341 (2021).
- [45] A. Buckley, J. Ferrando, S. Lloyd, K. Nordström, B. Page, M. Rüfenacht, M. Schönherr, and G. Watt, *Eur. Phys. J. C* **75**, 132 (2015).
- [46] C. Aidala et al. (PHENIX), *Phys. Rev. D* **99**, 072003 (2019).
- [47] TMD fits, <https://mapcollaboration.github.io>.